White Matter Fiber Tractography Via Anisotropic Diffusion Simulation in the Human Brain

Ning Kang, Jun Zhang*, Eric S. Carlson, and Daniel Gembris

***Abstract*—A novel approach to noninvasively tracing brain white matter fiber tracts is presented using diffusion tensor magnetic resonance imaging (DT-MRI). This technique is based on successive anisotropic diffusion simulations over the human brain, which are utilized to construct three dimensional diffusion fronts. The fiber pathways are determined by evaluating the distance and orientation from the fronts to their corresponding diffusion seeds. Synthetic and real DT-MRI data are employed to demonstrate the tracking scheme. It is shown that the synthetic tracts are accurately replicated, and several major white matter fiber pathways can be reproduced noninvasively, with the tract branching being allowed. Since simulating the diffusion process, which is truly a physical phenomenon reflecting the underlying architecture of cerebral tissues, makes full use of the diffusion tensor data, including both the magnitude and orientation information, the proposed approach is expected to enhance robustness and reliability in white matter fiber reconstruction.**

***Index Terms*—Anisotropic diffusion simulation, diffusion tensor MRI, fiber tractography.**

I. Introduction

DIFFUSION tensor magnetic resonance imaging, or DT-MRI, is an extension of conventional MRI with the added capability of tracking and measuring the random motion of water molecules in all three dimensions, usually referred to as self-diffusion or "Brownian motion." It is known that water diffusion is anisotropic in brain white matter. The significant anisotropy present in white matter reveals microscopic properties of the anatomy of the nerve fibers by the fact that water tends to diffuse predominantly along the long axis of the fibers. The longitudinally oriented tissue structures, the densely packed axons and in particular their membranes, which are widely assumed to be the main barrier for water diffusion, hinder diffusion perpendicular to the fibers [1]. DT-MRI is sensitive to this anisotropy and is able to characterize it by noninvasively quantifying and assessing the self-diffusion of water *in vivo*. The information concerning the local orientation of fibers, extracted from the water anisotropic diffusion in white matter, forms the basis of utilizing DT-MRI to track fiber pathways and build connectivity maps *in vivo*. The water diffusion behavior elucidated by the diffusion tensor imaging reflects the directional organization of the underlying white matter microstructure. DT-MRI characterizes the behavior on a voxel-by-voxel basis and for each voxel, the diffusion tensor yields the diffusion coefficient corresponding to any direction in space [2]. The direction of the greatest diffusion can be determined by evaluating the diffusion tensor in each voxel, which corresponds to the dominant axis of the white matter fiber bundles traversing the voxel. This has been validated to be the case, for instance, in the optic tract of the rat using manganese-enhanced MRI tracing techniques [3].

Typical fiber tracking schemes reconstruct the pathways of white matter tracts by starting from a seed voxel and tracing them down in a voxel-by-voxel manner, using an estimate of the local fiber orientation determined by the principal eigenvector in each voxel. At each voxel, the principal eigenvector, which is the one corresponding to the largest eigenvalue generated by the eigen decomposition of the diffusion tensor, is aligned with the mean fiber direction in that voxel. Hence, trajectories can be produced by integrating the principal eigenvector field, which are expected to coincide with the course of the white matter fiber bundles. Attempts have been made to trace the neural fiber pathways by this technique [4]–[7] and very impressive results on major fiber structures are exhibited. Those approaches are sometimes referred to as streamline tracking techniques, stemming from their similarity to computing flow streamlines from the velocity fields in fluid dynamics.

The streamline-type techniques appear to give excellent results in many instances if the principal eigenvector field is smooth. However, it suffers from a couple of significant limitations [8]–[10], particularly those related to the effects of noise and partial voluming. The vector field is error prone in that the noise in DT-MRI data will influence the direction of the principal eigenvector, yielding an accumulation of orientational errors and, thus, an erroneous fork of the trajectory reconstruction process. The partial volume effects [11], on the other hand, will cause it to run into trouble in tracking fibers correctly and reliably through the primary eigenvector field in regions of fiber crossing, branching, or merging, which renders a complicated averaging of multiple fiber populations within a single voxel. Since the current resolution of DT-MRI is 1–4 mm while the

Manuscript received February 2, 2005; revised May 19, 2005. This work was supported in part by the U.S. National Science Foundation under Grant CCR-9988165, Grant CCR-0092532, and Grant ACR-0202934; in part by the U.S. Department of Energy Office of Science under Grant DE-FG02-02ER45961; in part by a University of Kentucky Research Support grant; and in part by the Landesstiftung Baden-Württemberg, Germany under the "Elite support program for postdocs 2003". The Associate Editor responsible for coordinating the review of this paper and recommending its publication was N. Ayache. *Asterisk indicates corresponding author.*

N. Kang is with the Department of Computer Science, University of Kentucky, Lexington, KY 40506-0046 USA.

*J. Zhang is with the Department of Computer Science, University of Kentucky, 773 Anderson Hall, Lexington, KY 40506-0046 USA (e-mail: jzhang@cs.uky.edu; http://www.cs.uky.edu/~jzhang).

E. S. Carlson is with the Department of Chemical Engineering, University of Alabama, Tuscaloosa, AL 35487-0203 USA.

D. Gembris is with the South German Brain Imaging Center, Institute for Computational Medicine Mannheim/Heidelberg, University of Mannheim, D-68131 Mannheim, Germany.

Digital Object Identifier 10.1109/TMI.2005.852049

diameter of nerve fibers is in the magnitude of μm, it is difficult for the measured diffusion tensor to describe such entangled structures in those areas, making it undesirable to do fiber tracking by simply tracing down the principal eigenvector field.

A variety of methods have been proposed aiming to alleviate the effect of these limitations with more information incorporated and interpreted from the diffusion tensor data. The tracking algorithm presented in [8] uses a deflection term obtained from the diffusion tensor to improve the image noise immunity. The tracing scheme of [9] is based on a regularized fiber orientation map computed from a bending-energy model, partly overcoming the proneness to inaccurate forks. Taking into account the uncertainty of fiber direction, probabilistic and statistical approaches have been developed to rebuild the brain anatomical connections using regularized stochastic modeling [12], linear state space models [13], and Monte-Carlo type methods [14]–[16]. These methods introduce the possibility with varying degrees to mitigate the effects of fiber crossing and diverging as well as the sensitivity to noise. However, the techniques mentioned above are restricted to reconstruct the connectivity as a one-to-one mapping between points in different regions since they produce a single path for each starting point, potentially leading to a considerable loss of information. The fast marching methods based on level set theory, which models the evolution of an interface or front over time, have been applied in the context of fiber-tracking [17] to remedy the limitation. Another front evolution algorithm with the same capability of handling such situations is proposed in [18], which utilizes the fiber orientation density function to evolve the front and, thus, reconstruct fiber tracts. The level set method has also been used to implement other tracking algorithms based on diffusive similarity [19], the fiber orientation likelihood distribution [20], and Riemannian manifold and metric tensor [21], [22] to better deal with noise contamination and ambiguous diffusion tensors.

Most of the existing tracking techniques solely employ the orientation information carried by the diffusion tensor, totally ignoring the influence of the diffusion strength or magnitude of the tensor, which contains information about the strength of the water diffusion. A more robust way to determine the fiber network from diffusion tensor data is to conduct simulations of water diffusion over the brain, in which the magnitude of tensors plays an indispensable role. The diffusion is anisotropic and governed by the diffusion equation, where fiber bundles are assumed to proceed along the direction in which the diffusion is the greatest. The fiber tracking method presented in this paper exploits simulations of the diffusion process, through the solutions to the anisotropic diffusion equation.

The idea of studying brain connectivity by way of simulating the anisotropic diffusion has been preliminarily explored in [22]–[24], and [25] further extends the diffusion equation to a diffusion-convection equation by adding a convection term. However, there is no (or at best limited) attempt at determining the route of fiber pathways and connectivity between anatomically or functionally defined regions in the brain using this method, although the concentration or flow field over the brain is calculated. The technique in the current work relies on successive anisotropic diffusion simulations over the whole brain, which are utilized to construct three dimensional diffusion fronts. The next voxel, where a seed (an initial concentration value) will be placed, is located on the diffusion front which is created by the diffusion process initiated from the previous seed voxel. It is selected in terms of the fact that the higher the diffusion rate, the longer the distance that will be traveled within the same amount of time, as well as the orientation information from itself and its neighboring voxels. The fiber pathways can be determined by evaluating the distance and orientation of the vector from voxels on the fronts to their corresponding diffusion seeds.

We introduce in detail the diffusion equation-based fiber tracking algorithm in the next section. Experimental results with both synthetic and real DT-MRI data are presented in Section III. Section IV contains a discussion on the relation between our tracking method and the other competing methods. A brief summary is included in Section V.

II. Methods

A. Data Acquisition and Processing

Real diffusion tensor data were acquired from a single healthy subject at the Institute for Medicine, Jülich Research Center, Jülich, Germany. A Siemens Magnetom Vision 1.5 T scanner was used to do the measurement using single-shot spin-echo echo planar imaging with the following parameters: $\mathrm{TR} = 15$ s; $\mathrm{TE} = 100$ ms; resolution: 96×128; plane orientation: transversal; Field of View (FoV): 240×240 mm^2; slice thickness: 5 mm; number of slices: 16. The diffusion weighting corresponded to the Stejskal-Tanner gradient scheme [26] (b-factor: approximately 1000 s/mm^2). The gradient direction angles ϕ_i and θ_j were chosen as multiples of 22.5° ($\phi_i = i \cdot 22.5°, \theta_j = j \cdot 22.5°$). For the suppression of eddy-current artifacts the employed sequence included a zero and first order phase correction [27], [28]. The *non*-diffusion weighted images ($b = 0$ s/mm^2) actually had a small diffusion weighting of about $b \approx 50$ s/mm^2, which was neglected in the computation of the diffusion tensors, but which is sufficient to significantly reduce sensitivity against blood flow changes.

For the data acquisition, the measurements were distributed over 22 pulse sequences (four different weightings per sequence: the first with $b = 0$ s/mm^2 and the other three with $b = 1000$ s/mm^2, but with three different gradient directions resulting in 66 gradient directions in total), which were repeated 10 times to increase the signal-to-noise ratio. This resulted in blocks of 4×10 data sets for each sequence. The averaging was performed in postprocessing with any potential head motion during the repetitions neglected (no motion compensation). The measurement was distributed over three sessions on different days. For the averaged data sets, however, a motion correction was performed using the SPM99 software package (http://www.fil.ion.ucl.ac.uk/spm), where the largest displacements were due to changes in head position between different sessions. (Some alternative DT-MRI motion correction and registration strategy is discussed in [29].) The total measurement time was about eight hours including the latency times for image reconstruction that could not be postponed to

the end of the measurement or performed off-line for technical reasons.

The resolution of the original calculated tensor data volume is $128 \times 128 \times 16$ with each voxel having size $2.5 \times 2.5 \times 7.5$ mm^3 defined on a Cartesian mesh. It has been recomputed using trilinear interpolation, resulting in a uniform voxel size of (2.5 mm)^3.

B. Anisotropic Diffusion in Brain

In the diffusion-based fiber tractography, we treat the whole 3-D brain volume as a system with anisotropic diffusion properties, over which a virtual water diffusion process is simulated. A thorough discussion about the diffusion process and related transport mechanisms in brain can be found in [30]. Anisotropic systems are those that exhibit a preferential spreading direction while isotropic systems are those that have no preference. According to Fick's macroscopic law of diffusion, which describes the physical behavior of the diffusion process, the flux, J, is related to the concentration, ρ, by

$$J = -D\nabla\rho \tag{1}$$

where D is the so-called diffusion coefficient. This equation states that the concentration gradient $\nabla\rho$ causes the flux J which aims to compensate for this gradient. Substituting (1) into the continuity equation

$$\frac{\partial\rho}{\partial t} + \nabla \cdot J = 0$$

which expresses the conservation law of mass, we end up with the equation governing the anisotropic diffusion process

$$\frac{\partial\rho}{\partial t} = \nabla \cdot (D\nabla\rho) \tag{2}$$

where t is the independent time variable. This equation says that over the time, the rate of change in concentration is proportional to the divergence of the flux.

For a homogeneous isotropic environment, D is a scalar-valued constant and the directions of J and $\nabla\rho$ are parallel. In the presence of anisotropy, the flow field does not follow the concentration gradient directly. The diffusion coefficient D, therefore, has to be characterized as a second-order tensor, which delivers a complete description of the molecular mobility along each direction and the correlation between these directions. The diffusion tensor is represented by a three-by-three symmetric (semi)positive definite matrix, namely,

$$D = \begin{pmatrix} D_{xx} & D_{xy} & D_{xz} \\ D_{yx} & D_{yy} & D_{yz} \\ D_{zx} & D_{zy} & D_{zz} \end{pmatrix}$$

where $D_{xy} = D_{yx}, D_{xz} = D_{zx}, D_{yz} = D_{zy}$, and the subscripts xx, xy, xz, etc., denote the values of the individual coefficients in the matrix that can be seen as the influence from directions in the input (being the concentration) on the various directions in the output (being the flux).

Since the brain tissue is not only anisotropic but also heterogeneous, the diffusion tensor D in such a case depends on the position in space and, thus, the spatial derivatives of the tensor components D_{xx}, D_{xy}, D_{xz}, etc., must be introduced. In a Cartesian coordinate system, for a given position in the tensor volume, (2) is written as

$$\begin{aligned} \frac{\partial\rho}{\partial t} = &\frac{\partial}{\partial x}\left(D_{xx}\frac{\partial\rho}{\partial x} + D_{xy}\frac{\partial\rho}{\partial y} + D_{xz}\frac{\partial\rho}{\partial z}\right) \\ &+ \frac{\partial}{\partial y}\left(D_{yx}\frac{\partial\rho}{\partial x} + D_{yy}\frac{\partial\rho}{\partial y} + D_{yz}\frac{\partial\rho}{\partial z}\right) \\ &+ \frac{\partial}{\partial z}\left(D_{zx}\frac{\partial\rho}{\partial x} + D_{zy}\frac{\partial\rho}{\partial y} + D_{zz}\frac{\partial\rho}{\partial z}\right). \end{aligned} \tag{3}$$

C. Constructing Successive Diffusion Fronts

The fundamental idea behind our fiber tractography is to perform successive diffusion simulations over the brain stemming from a series of selected starting voxels where a seed is placed. With certain thresholds satisfied, the starting voxels, or diffusion root nodes, are dynamically picked up from the nodes on the three dimensional diffusion interfaces or fronts produced by previous rounds of the diffusion simulation. Thus, the first step to reconstruct fiber pathways starting from a prechosen root node $s \in \mathbb{R}^3$ (where $\mathbb{R}$ is a set of real numbers) involves the simulation of diffusion starting from a seed in this voxel. The virtual concentration seed of water spreads from the root node through neighboring nodes, within a limited amount of time, forming a diffusion front which is the surface of a diffusion volume containing nodes with nonzero[1] concentration values. The expansion of the diffusion volume originated from the root voxel is achieved by integrating the anisotropic diffusion equation (2) through the whole brain over a certain amount of time, subject to the following initial condition

$$\rho|_{t=0} = \begin{cases} 1, & \text{at the root voxel} \\ 0, & \text{otherwise.} \end{cases} \tag{4}$$

For the boundary condition of (2), we assume that the physical system containing the brain is insulated, i.e.,

$$(D\nabla\rho) \cdot \boldsymbol{n} = 0 \tag{5}$$

where $\boldsymbol{n}$ is the outward-pointing vector normal to the boundary surface. This corresponds to the Neumann condition, which implies that the normal part of the gradient of the concentration on the boundary is zero, in other words, nothing escapes out of the domain.

The solution of the time-dependent diffusion equation (2) is not trivial since the human brain structure displays anisotropic, inhomogeneous diffusion properties. We have recently developed and implemented an unsteady state anisotropic diffusion solver framework, which is adapted to the cerebral circumstance and has been designed for both sequential and parallel computing environments [31], [32]. In the current paper, we solve sequentially the governing diffusion equation (2) by resorting to the established computational framework. Since the tensor data set used in the simulation is processed and stored on a Cartesian mesh, we do this by first discretizing the diffusion equa-

[1]For zero concentration values, we actually mean values close to zero. A threshold can be applied to determine zero and nonzero values.

tion (3) on this grid using finite difference approximations. The central difference scheme in space and the backward differentiation formula in time are applied to approximate the spatial derivative and time derivative terms in (3), respectively. The discretization of (3) and its boundary condition (5) on the Cartesian grid generates a large scale system of semi-explicit differential-algebraic equations (DAEs). We then solve the initial value problem for the resulting system of DAEs by way of a high performance implicit differential-algebraic (IDA) solver, using the scaled preconditioned generalized minimal residual (GMRES) iterative method with incomplete LU (Lower-Upper) factorization preconditioning applied. The IDA solver is one of the software packages contained in the Advanced CompuTational Software (ACTS) collection (http://acts.nersc.gov).

In order to construct the diffusion front propagated from a root voxel where a seed has been placed, we only integrate (3) over a fine-tuned amount of time through the whole brain using the time-dependent diffusion solver framework described above. The length of the integration time is determined in a way such that without the loss of revelations of the anatomical properties of the underlying nerve fibers, the number of voxels swept by the diffusion process initiated from the root voxel should be as small as possible. In fact, this value is chosen according to several factors including the magnitude of the tensor data, the spatial resolution of the computational grid, and the initial concentration at the root voxel. Once the time integration procedure is completed, a discrete approximation to the diffusion front can be calculated in terms of whether the concentration value is zero in a voxel. This is the ideal case though, we have to set a threshold to define zero concentration in the actual implementation. Thus, all nodes in the computational grid can be partitioned into two groups, one with zero concentration value and the other with nonzero value. Let $V(r)$ denote the set of voxels that have nonzero concentration values, corresponding to the nodes in the diffusion swept volume, where r is the position of the root node. For each member of $V(r)$, we consider its surrounding 6 closest neighboring nodes in a $3 \times 3 \times 3$ kernel. Let i, j, k index the relative coordinates of the 6 nearest neighbors to r with $i, j, k \in \{-1, 0, 1\}$. If $F(r)$ is the set of voxels that form the diffusion front of r, then for any node $p \equiv (p_x, p_y, p_z) \in V(r)$, we define

$$p \in F(r) \text{iff} \begin{cases} \exists\, i, & (p_x - i, p_y, p_z) \notin V(r), \text{ or} \\ \exists\, j, & (p_x, p_y - j, p_z) \notin V(r), \text{ or} \\ \exists\, k, & (p_x, p_y, p_z - k) \notin V(r). \end{cases} \tag{6}$$

Fig. 1 shows a simulated concentration distribution map of the anisotropic diffusion in the human brain by using the aforesaid diffusion tensor data. The simulated result is derived from solving (3) under the initial condition (4) and boundary condition (5). Demonstrated in Fig. 2 is an illustration of the discrete approximation to a diffusion front emerging from a root voxel r.

Before presenting the algorithm to build up successive diffusion fronts originated from the starting voxel s, we set up a queue Q, a first-in first-out data structure, to store and handle the dynamically produced front nodes. Q is initialized to contain just the starting node s, i.e., $Q = \{s\}$ before the start of the

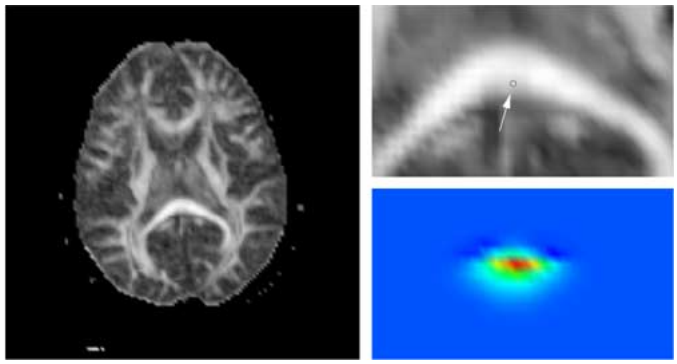

Fig. 1. Illustration of the anisotropic diffusion process originated from a starting voxel where a seed is placed. Left: an axial map of the fractional anisotropy (fa) in grey scale, shown for anatomical reference. Upper-right: a close-up of the splenium (fa map) with the starting voxel indicated as a black circle pointed to by a white arrow. Lower-right: a cross-section image of the concentration distribution field corresponding to the close-up fa map, where the warmer colors (like red and yellow) represent larger concentration values, while the cooler colors (like blue and green) stand for smaller values.

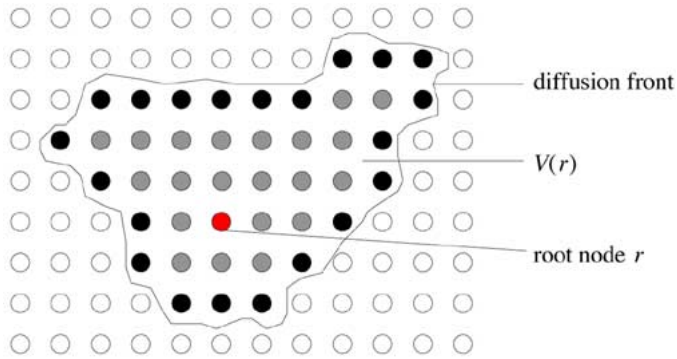

Fig. 2. The illustration of the discrete approximation to a diffusion front, which borders the diffusion-swept volume $V(r)$ containing the node r (shown in red) as the root where a seed is diffused and grey nodes with nonzero concentration value. Those originally grey nodes that satisfy the condition (6) are colored black, which are used to approximate the front. The white nodes are the ones with zero concentration value.

successive diffusion simulations; thereafter, Q always contains the set of diffusion front nodes. We also define a set C to bear a number of criteria, which controls the way of determining the connection of fiber pathways. A detailed description of this set, comprising the choice of the thresholds, will be given shortly in Section II-D.

Once $F(r)$ is computed for the root node r, we further apply the criteria in C to the nodes of $F(r)$ and pick up those that meet the corresponding thresholds. We define $I(r)$ to be the set of nodes selected from $F(r)$ that are in accordance with those criteria in C, i.e.,

$$I(r) = \{p \in F(r) \,|\, p \text{ meets all the criteria in } C\}.$$

$I(r)$ is then appended to the tail of the queue Q. The current head node of Q is removed from the queue and is considered to be a new root r' from which a seed is diffused, and its diffusion front $F(r')$ is calculated in the same way as that of $F(r)$ by solving and integrating (3) over a certain amount of time through the whole brain. As the derivation of $I(r)$, the set $I(r')$ is determined as well by checking each member of $F(r')$ based upon the criteria in C, then it is added to the tail of Q. We continue in

this way by repeatedly taking off the head node of Q and processing it as a new root to diffuse a seed over it, until the queue becomes empty. The following algorithm outlines the procedure for constructing successive diffusion fronts.

Algorithm 1 Construct successive diffusion fronts.

1: specify a starting node s
2: initialize Q such that $Q = \{s\}$
3: **while** Q is not empty **do**
4: remove the head node r off Q and take it as a root
5: get $V(r)$ by solving the anisotropic diffusion equation (3) with the initial and boundary conditions (4) and (5) imposed
6: compute $F(r)$
7: determine $I(r)$ and append it to the tail of Q
8: **end while**

D. Determining Fiber Pathways

During the construction of successive three dimensional diffusion fronts, the connection between a diffusion root node r and the nodes in its diffusion front $F(r)$ may determine the possible routes of the fiber tract going through both r and $F(r)$. As mentioned earlier, the connectivity is regulated by the criteria set C, which determines the members of $I(r)$. The fiber pathways passing the node r and its diffusion front can be obtained by just connecting r and the nodes in $I(r)$. Obviously, fiber branching is achieved in this way since the size of the set $I(r)$ can be greater than 1 such that the tracking route is allowed to split at r.

There are seven criteria in C used to evaluate the information about distance and orientation between the root r and its front nodes in $F(r)$. Let $C = \cup_{i\in\{1,\ldots,7\}}\{c_i\}$.

The first criterion, c_1, is the threshold for distance ratio (dr) measure, which is defined as

$$dr = \frac{d}{d_{\max}}$$

where $d = ||\boldsymbol{v}(r)||$ is the Euclidean distance in $\mathbb{R}^3$ of two points, connected by the vector $\boldsymbol{v}(r)$ pointing from r to a node in $F(r)$, while d_{max} is the maximum value among the d's. The path reconstruction of white matter fiber bundles, which are assumed to proceed along the direction in which the diffusion is fastest, can be accomplished by our tracking approach, thanks primarily to the fact that the faster the diffusion rate is, the longer the distance will be traversed within the same amount of time by the diffusion medium, water. If we just follow the direction with the longest distance, branching of fiber pathways cannot be handled adequately in the reconstruction. Moreover, both the error and noise in measurement and the partial voluming can deflect the tracking from the true path and orientation. In order to accommodate the branching tracts and minimize the possibility of deviation from the fiber trajectories, we choose a value between 0.7 and 0.85 for the threshold c_1 and consider the cases with $dr \geq c_1$, following a few more directions with less fast diffusion rates rather than only the orientation with the fastest diffusion. By this way, the tracking procedure is likely to be more robust and reliable in noisy measurements.

We set the second criterion c_2 to be a threshold of an invariant anisotropy index, the fractional anisotropy (fa), which is defined as [33]

$$fa = \sqrt{\frac{(\lambda_1-\lambda_2)^2+(\lambda_2-\lambda_3)^2+(\lambda_3-\lambda_1)^2}{2(\lambda_1^2+\lambda_2^2+\lambda_3^2)}}$$

where λ_1, λ_2, and λ_3 (assuming $\lambda_1 \geq \lambda_2 \geq \lambda_3$) are the three eigenvalues of the 3×3 symmetric diffusion tensor D. fa assesses the fraction of the magnitude of D that can be attributed to anisotropic diffusion. It takes on values between 0 (fully isotropic diffusion) and 1 (infinite anisotropy). If the fa value of any voxel p falls below c_2, p will not be considered as a diffusion root node, which prevents erroneous trajectory propagation into the grey matter structures and cerebrospinal fluid in the brain. A value of 0.1 or 0.2 for c_2 has proved to serve the purpose in this study.

The next four criteria, from c_3 to c_6, are called smoothness criteria which are used to judge the coherence of fiber directions along the reconstructed trajectories passing through r. The coherence measure depends on the inner products of four pairs of unit vectors (ip_1, ip_2, ip_3, ip_4), which are expressed as

$$ip_1 = \hat{\boldsymbol{v}}(r)\cdot\hat{\boldsymbol{v}}(\pi(r)) \tag{7}$$
$$ip_2 = |\hat{\boldsymbol{v}}(r)\cdot\boldsymbol{e}_1(r)| \tag{8}$$
$$ip_3 = |\hat{\boldsymbol{v}}(r)\cdot\boldsymbol{e}_1(f)| \tag{9}$$
$$ip_4 = |\boldsymbol{e}_1(r)\cdot\boldsymbol{e}_1(f)| \tag{10}$$

where $\hat{\boldsymbol{v}}(r)$ and $\hat{\boldsymbol{v}}(\pi(r))$ are normalized vectors, $\hat{\boldsymbol{v}}(r) = \boldsymbol{v}(r)/||\boldsymbol{v}(r)||, \hat{\boldsymbol{v}}(\pi(r)) = \boldsymbol{v}(\pi(r))/||\boldsymbol{v}(\pi(r))||$. Here, $\pi(r)$ is called the predecessor voxel of r, i.e., $r \in I(\pi(r))$, and $\boldsymbol{v}(\pi(r))$ is the vector pointing from $\pi(r)$ toward r. $\boldsymbol{e}_1(r)$ and $\boldsymbol{e}_1(f)$ are the principal eigenvectors (corresponding to the largest eigenvalue λ_1 of the diffusion tensor D) at the voxel r and $f \in F(r)$, respectively. $c_3, \ldots, c_6$ are the thresholds for $ip_1, \ldots, ip_4$, respectively. Indeed, $ip_1, \ldots, ip_4$ measure the angles between orientations of those vectors, as shown in Fig. 3, and (7)–(10) also imply that $ip_1 \in [-1, 1]$ and $ip_2, ip_3, ip_4 \in [0, 1]$. Since $\boldsymbol{v}(\pi(r))$ is an established vector implying the presence of a trajectory passing in this direction, the information contained in ip_1 is exploited to appraise the next possible fiber path orientation aligned with $\boldsymbol{v}(r)$ by examining the degree of co-linearity between $\boldsymbol{v}(\pi(r))$ and $\boldsymbol{v}(r)$. The thresholds for ip_2, ip_3, and ip_4, which are chosen to be the same value for each testing case ranging from 0.55 to 0.85, are used to guard the local directional coherence of the estimated tract and curb the trajectory from following unlikely pathways. c_3 is set to be a value between 0.7 and 0.8 such that the tracking direction could be pushed forward consistently and smoothly without erratically turning backward, preventing the computed path from sharp transition.

The last criterion, c_7, is the maximum number of voxels $I(r)$ is allowed to have if there are more voxels than expected satisfying all previous six criteria. The elements of $I(r)$ are determined by checking each voxel in $F(r)$ in a nonascending order of the distance ratio to see if it meets all aforementioned six criteria until the prescribed capacity of $I(r)$ is reached. The purpose of setting this threshold is to control the total computational

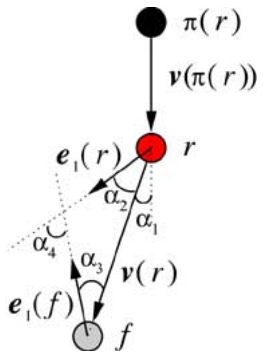

Fig. 3. Transition smoothness of fiber trajectory relies on the size of the angles $\alpha_1, \alpha_2, \alpha_3$, and α_4, which are determined by ip_1, ip_2, ip_3, and ip_4, respectively.

time for doing the successive diffusion simulations. In the current work $c_7 = 5$.

Aimed at recovering the fiber pathways after the construction of diffusion fronts, each voxel p in the voxel grid owns a memory of its predecessor voxel, $\pi(p)$, where $p \in I(\pi(p))$. In the current implementation of the tracking scheme, $\pi(p)$ is the sole predecessor of p if there is one. Thus, back propagation from the voxels on the diffusion fronts by following continuously the corresponding predecessor voxels may lead to paths that merge to the starting voxel s. This merging corresponds to the procedure that can be viewed in the reverse direction as fiber tracts branch outwards from s. Finally, the pathways are smoothed out by using B-spline least-square approximations. By combining Algorithm 1 with the back propagation process, the diffusion simulation based fiber tracking algorithm is presented as follows:

Algorithm 2 Fiber tracking by diffusion simulations.

1: specify a starting voxel s
2: build successive diffusion fronts (Algorithm 1)
3: record π values for voxels during front construction
4: retrieve fiber pathways using back propagation

III. Results

A. Synthetic Diffusion Tensor Data

In order to assess fidelity and robustness of the tracking algorithm, we generated synthetic DT-MRI data with a regular voxel size of $(1\ \text{mm})^3$, where the true path of a fiber tract is known. The tensor field was constituted from an anisotropic tensor dataset and an isotropic tensor dataset taken out of real DT-MRI data. The shape of the diffusion tensor in synthetic fibers was described by the anisotropic one such that $\lambda_1{:}\lambda_2{:}\lambda_3$ was approximately 2.5:1:1, while the isotropic one was used to forge the background of the simulated tensor field. The vector field for fiber orientations was derived by sampling discretely the trajectories which were analytically defined. To make the simulated field more realistic, an approximation to Rician noise [34] was added in the diffusion-weighted images which were calculated from the Stejskal-Tanner equation using the gradient sequence in [35] and a b-value of 1000. The values of the diffusion coefficients are around 5.0×10^{-9} m^2/s and the noisy realization

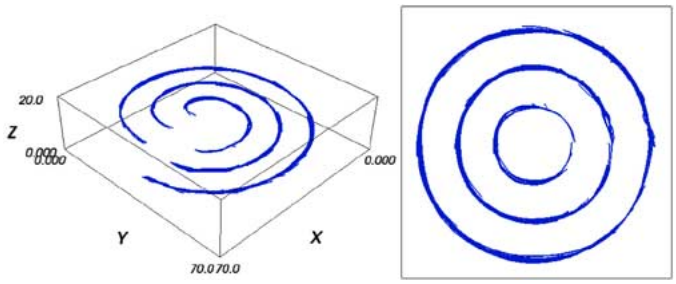

Fig. 4. Tracing results on single-turn helical tracts of varying radii. Left: 3-D view. Right: A projection onto the X-Y plane.

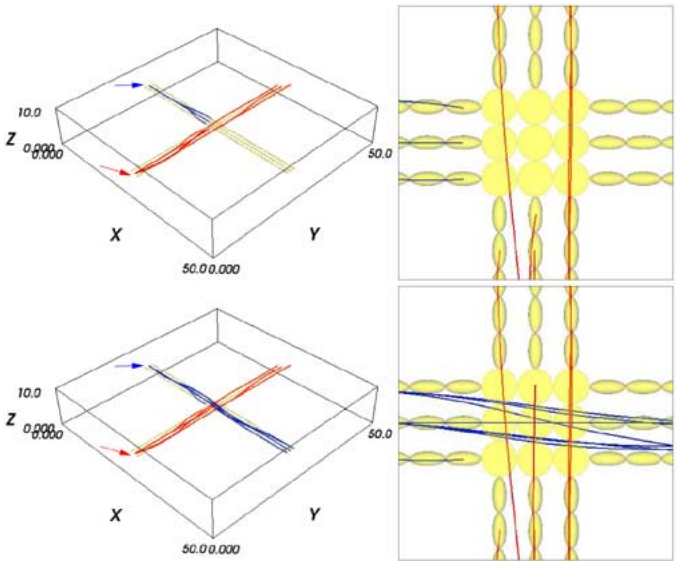

Fig. 5. Tracing results on crossing tracts with different local coherence thresholds applied. The two crossing straight-line fiber bundles are illustrated as diffusion tensor ellipsoid map, showing an oblate shape for tensors in crossing regions. The blue and red pathways yielded by the algorithm are initiated from a single voxel pointed to by a blue and red arrow, respectively. Upper: $c_4 = c_5 = c_6 = 0.75$. Lower: $c_4 = c_5 = c_6 = 0.7$.

led to a signal-to-noise ratio of 10. A compact analytic solution to the Stejskal-Tanner equation [35] was employed to yield the desired noisy synthetic diffusion tensor data.

Three single-turn helical fiber bundles have been synthetically generated in a $70 \times 70 \times 20$ grid with radius being 30 mm, 20 mm, and 10 mm, respectively. For each helix, trajectories are traced from a single voxel located at the lower end of the tract. Fig. 4 presents the tracking results, showing that the simulated helical curves are accurately reproduced. It is also evident from the plots that the tract-following algorithm barely exhibits any performance degradation when the diameter of the helical curve decreases.

Fig. 5 delineates the tracing results on crossing fiber tracts synthetically constructed with two straight-line fiber bundles running along the X- and Y-axis, respectively, in a $50 \times 50 \times 10$ grid. The tracking, being released from a single starting voxel on one end of each tract, is carried out under different local coherence thresholds with the remaining criterion settings staying the same. As seen from the plots in the first row of Fig. 5 which show the computed tracks with $c_4 = c_5 = c_6 = 0.75$, the tracking along the X-axis (the blue paths) stops right before the crossing region, while the whole ideal tract in the direction of

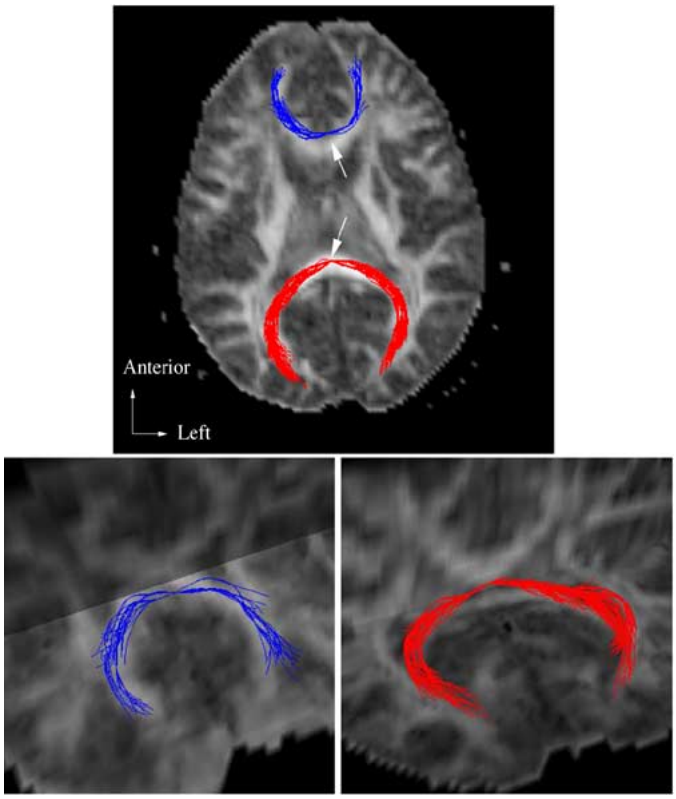

Fig. 6. Fiber pathways of corpus callosum computed from two starting voxels located in the genu (fibers are colored in blue) and splenium (fibers are colored in red), as pointed to by white arrows, respectively. Upper: Fibers are viewed from the inferior direction, overlaid on an axial fa map. Lower-left: A 3-D superior-anterior view of the genu fibers, shown together with axial and coronal fa maps. Lower-right: A 3-D superior-posterior view of the splenium fibers, shown together with axial and coronal fa maps.

Y-coordinate (the red paths) is faithfully followed by the algorithm. With a relaxed setting for the local coherence threshold, $c_4 = c_5 = c_6 = 0.7$, it turns out that both tracts are closely replicated by the algorithm which penetrates the area of planar tensors along the X-axis and allows more paths along the Y-axis to get through, as displayed in plots in the second row of Fig. 5. One can also observe that there is no jump or divergence from one tract to another over the crossing area under the stated threshold settings.

B. Real DT-MRI Data

We now demonstrate the tracking approach by exploring its ability to reproduce some well-known courses of white matter structures in the human brain. The reconstructed fiber trajectories launched from different starting points are overlaid on grey-scale maps of the fractional anisotropy for anatomical reference, where bright grey-scale regions reflect high diffusion anisotropy.

The first of the fiber pathways considered as an example of the method is the corpus callosum tract, which interconnects the left and right cerebral hemispheres and has the highest anisotropy and temperate curvature. Fig. 6 shows the reconstructed fiber tracts stemming from two starting voxels located in the anterior and posterior portions of the corpus callosum, i.e., the genu and splenium, respectively. The tracking from the two starting voxels results in fibers traversing the genu and splenium and

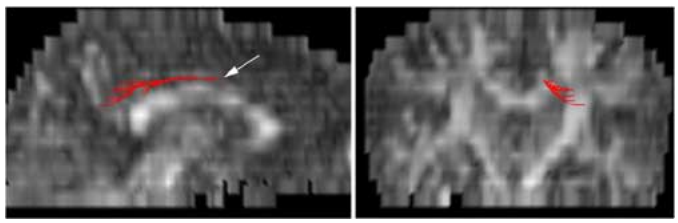

Fig. 7. Fiber pathways of cingulum calculated from a starting voxel which is slightly above the body of the corpus callosum and labeled by a white arrow in the right front lobe. Left: Viewed from right, overlaid on a midline sagittal fa map. Right: A posterior view, shown together with a coronal fa map.

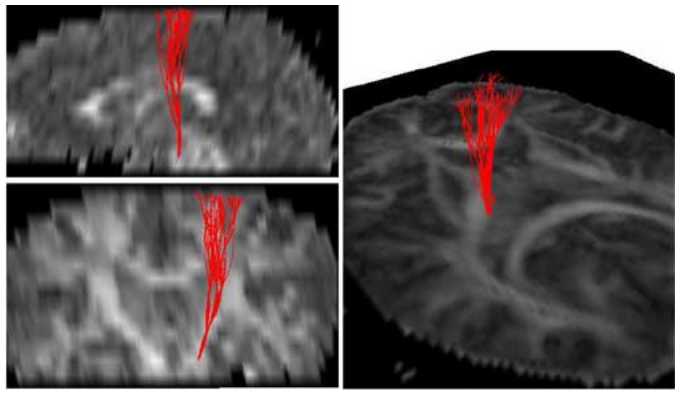

Fig. 8. Fiber pathways of corticospinal tract computed from a starting voxel positioned approximately in the left portion of the base of the pons area. Upper-left: Viewed from left, overlaid on a sagittal fa map at the midline. Lower-left: Viewed from front, superimposed on a coronal fa map. Right: A 3-D view, shown together with an axial fa map.

running toward the frontal and occipital poles of the two cerebral hemispheres, respectively. The trajectories are traced following the curvature of the genu and splenium, exhibiting an arched shape, which is consistent with the known anatomy. It is evident from Fig. 6 that the diffusion-based tracking scheme allows for tract branching since the generated fiber trajectories start from a single point and then end up with multiple points, forming a number of branching pathways from one single starting voxel.

Depicted in Fig. 7 is another tracking example, which shows computed fiber pathways of the cingulum, a major tract constituting the limbic system. The reconstruction takes off from a single starting voxel lying within the white matter of the cingulate gyrus, slightly above the body of the corpus callosum in the right frontal lobe. The fibers generated run longitudinally along and above the corpus callosum to the posterior parietal lobe and the splenium.

The next example of the fiber tract reconstruction belongs to the system of projection pathways, which connects the cerebral cortex and the spine. More specifically, we have attempted to generate the fiber pathways for the corticospinal tract, which conveys impulses for cortical control of the voluntary movements. The tracking result of the projection traces is elucidated in Fig. 8. The estimate of this type of corticofugal fiber bundles is obtained by launching trajectories from a single starting voxel placed approximately in the left portion of the base of the pons area. The yielded pathways traverse superiorly through the posterior limb of the internal capsule and form the corona radiata, consistent with the route of the corticospinal tract. It is also apparent that the computed course of the fiber tract from

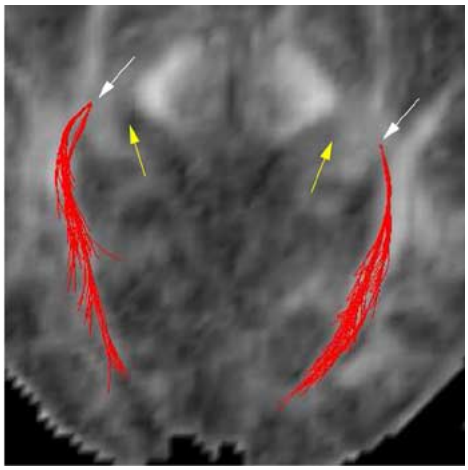

Fig. 9. Fiber pathways in the optic radiations, from two starting voxels (indicated by white arrows) lateral to each of the lateral geniculate nuclei (LGN). Fibers are viewed from top, overlaid on an axial fa map. The approximate positions of the LGN are pointed to by yellow arrows.

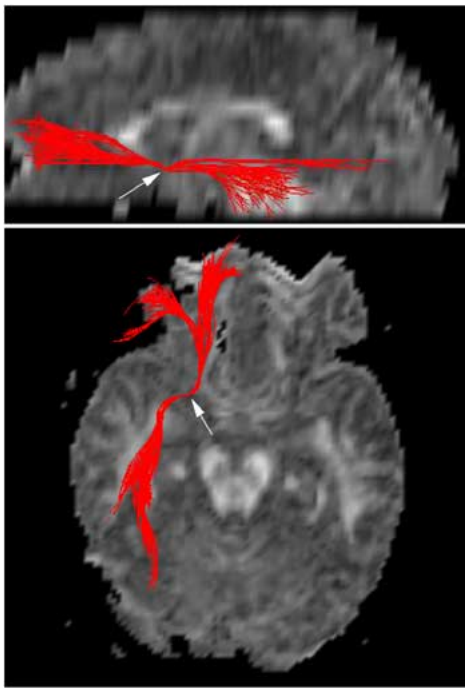

Fig. 10. Fiber pathways in the inferior occipitofrontal fasciculus, emerging from a starting voxel (labeled by a white arrow) in the junction area of the frontal and temporal lobes in the left hemisphere. Upper: Viewed from left, shown together with a midline sagittal fa map. Lower: Viewed from above, overlaid on an axial fa map.

the starting point branches into a couple of different cortical motor regions, including the medial and lateral parts of the primary motor cortex, the supplementary motor area, and the premotor cortex, as shown in Fig. 8. The projections to the pons area from the motor regions via the estimated corticospinal tract are in good agreement with the known anatomical connections.

The following demonstration of the tractography algorithm is to replicate the tract of optic radiations, or geniculo-calcarine visual projection, that relays visual information from the lateral geniculate nucleus (LGN) of the thalamus to the visual cortex. Two starting points, one for each of the cerebral hemisphere, are placed in the body of the optic radiations, lateral to the position of the LGN. The computed fibers of the optic radiations are displayed in Fig. 9, showing that each optic radiation arises from the starting voxel, sweeps posteriorly through the temporal lobe then the occipital lobe, and terminates in the region of the calcarine sulcus with branching traces. It is characteristic for the topology of the optic radiation that its spatial course runs in a medial-lateral orientation after coming out of the LGN and then changes to an anterior-posterior orientation, which is demonstrated by the tract behavior in [5], [17]. However, the portion of the optic radiation that runs in the medial-lateral direction between the LGN and the starting points is not identified in the current tracking result. This could be due to the insufficient spatial resolution in the superior-inferior direction of the original DT-MRI data acquisition.

Fig. 10 shows the result of the last experiment, in which we have traced one of the long association pathways, the tract of the inferior occipitofrontal fasciculus. The position of the starting voxel is located approximately in the junction area of the frontal and temporal lobes in the left hemisphere, from which the generated fasciculus fans out in both anterior and posterior directions. On one hand, the fasciculus runs anteriorly, radiating into cortical regions of the frontal lobe. On the other hand, it streams backward, branching into the temporal and occipital lobes. Apparently, the reproduced tract of the inferior occipitofrontal fasciculus connects the frontal cortex with the posterior temporal cortex and the occipital lobe.

IV. Discussion

We have tested the diffusion simulation-based tracking algorithm on real diffusion tensor MRI data as well as on synthetically generated noisy tensor fields. The algorithm performs very well on the simulated data, tracing accurately through the helical and crossing tracts. The experiments on real brain data include the corpus callosum, the cingulum, the corticospinal tract, the optic radiation, and the inferior occipitofrontal fasciculus, and the estimated pathways are largely faithful to the corresponding neuroanatomy known from postmortem dissections [36], [37] and compatible to those obtained by using other tracking approaches [4], [5], [7], [8], [17], [38]. The demonstration shows it is feasible to employ the diffusion-based tracking technique to noninvasively reconstruct white matter fiber tracts in the living human brain.

Previous work, as shown in [22]–[24], has attempted to perform fiber tracking by solving simplified variants of the general anisotropic diffusion equation (2). In the approach proposed in [23], a seed diffuses through the brain from a selected starting point by solving the full diffusion equation and the amount of concentration at some location is interpreted as a probability to reach that point. The work of [22] instead solves the steady-state diffusion equation with boundary conditions representing one source and one sink and then uses this information to calculate the steady-state flow field which is supposed to recover the underlying anatomical path between the source and sink. Both methods are completely different from our method to exploit the diffusion process, in which we construct successive three dimensional diffusion fronts to determine the fiber pathways by

evaluating the distance and orientation from the computed fronts to their analogous diffusion seeds. In [24], an anisotropic diffusion equation is solved, however, no effort has been made to show that the paths of fibers or the connections can be reconstructed between anatomical or functional regions of the brain.

Regarding the use of diffusion tensor data for unveiling the organizational patterns of white matter structures, the diffusion-based tractography has several potential advantages. First, as we have demonstrated, it has the similar desired capability of elucidating branching pathways naturally, giving a one-to-many mapping, like the fast marching approach [17] and the front evolution algorithm described in [18], which is an advantage over the streamline-based methods. As noticed in [17], without using some schemes such as making multiple interpolated starting points within the starting voxel, it is impossible for the existing streamline-based tracking methods to generate diverging fiber trajectories when the tracing starts from a single point, while with the use of these schemes, the density of trajectories will reduce and, thus, get subsequent connected regions undersampled. There is no such undersampling problem for the branching process in our tractography since the algorithm follows all branching pathways in the same manner, computing diffusion fronts consecutively. The fast marching technique is adopted in the context of the diffusion tensor domain to propagate fronts that evolve at a rate controlled by the principal eigenvector field. The front evolution algorithm employs the information provided by the fiber orientation density function. Compared to both approaches, the diffusion-based tractography relies on successive diffusion fronts constructed by a series of simulations of the diffusion process in the whole brain, which is a totally different mechanism exploited to do front propagations with a clear physical interpretation.

Another feature of our method is that it is likely to enhance the robustness and reliability in fiber reconstruction. Used as the basis for our tractography, performing simulations on the diffusion process, which is truly a physical phenomenon, is evident to help reveal the underlying tissue structures. The fiber reconstruction process is, thus, able to take into consideration the impact of the diffusion strength, as measured by the diffusion distance map, instead of fully counting on the orientation of the tensor in each voxel. As mentioned earlier, the noise of the imaging system will add uncertainty to the estimation of the diffusion tensor field and its eigenvectors. This effect will yield an accumulation of orientational errors and result in spurious trajectories when the tracing on white matter tracts is entirely dependent on the principal eigenvector field, as most of the streamline-based tracking methods and the fast marching tractography do. The diffusion-based tractography, however, has a lower chance to get affected by the noise. Since the anisotropic diffusion equation which governs the diffusion simulation is macroscopic, the noise effect is apt to get minimized or averaged out during the simulation procedure. More information, including the magnitude as well as the orientation of the tensors, is involved in determining fiber pathways, also helping palliate the sensitivity of the algorithm to noise.

Since our tractography process spreads diffusion over the brain regardless of whether an area is filled with anisotropic, oblate, or isotropic tensors, the method with appropriate threshold settings can greatly improve the handling of regions with crossing fibers or flat tensors, and make it more likely for the tracking process to slide through with correct pathways, as demonstrated in the synthetic crossing tracts, the corticospinal tract, and the cingulum. When the algorithm enters a region with planar tensors, if the diffusion tensor at a front voxel f is somewhat disc-shaped, it is possible that $\boldsymbol{e}_1(f)$, the principal eigenvector of f, gets orthogonal to the direction of $\boldsymbol{v}(r)$ or $\boldsymbol{e}_1(r)$ (see Fig. 3 for illustration). If the threshold c_5 or c_6 is set to be positive, which most often is the case, the tracking through voxel f will stop. However, one stop does not automatically terminate the whole tracking process since there may have other voxels available on the front which satisfy the threshold setting, making it stay on. A usual way for our method to assuage such a situation is to relax some of the thresholds such that more voxels on fronts will be available for evaluation, increasing the chance for the algorithm to behave correctly through the entangled area. The capability of capturing fiber crossings with this feature is made possible by the leap-frog tracking style of the algorithm, which leaps over a couple of voxels each time controlled by the diffusion simulation and measured by the distance traveled, instead of continuously assessing the very next neighboring voxel, which is easier for tracking algorithms to get stuck in intersecting areas. Although the technique has this potentiality, with relaxed thresholds imposed, it bears the risk of establishing more suspicious or even false crossing fiber connections in realistic and complicated cases, which has to be treated cautiously. But if the crossing structure is relatively simple and is known in advance, the algorithm seems to give reliable results, as proved in the simulated data as well as by the real data. Clearly, this approach is only an approximate solution to the complex problem of equivocal tensors, not yet a rigorous way to account for partial volume effects.

In fact, diffusion tensor imaging (DTI), as is used by our diffusion-based tracking method, is unable to truly resolve the crossing of multiple axon directions within a single voxel [11], [39]–[41]. Despite the fact that the information captured from DTI is limited by the second-order tensor model it applies, which assumes water molecules follow Gaussian diffusion in biological tissues, the tensor formalism is well accepted and its attributes can be obtained in a straightforward way. Furthermore, the macroscopic theory of Gaussian diffusion is modeled by Fick's first law (see (1)), which makes simulating the diffusion process by solving the diffusion equation (2) a natural fit-in to obtain information of the underlying fiber structure and connectivity. For those reasons, the tracking algorithm based on diffusion simulations is implemented to use the DTI data, which needs to be fed into the corresponding diffusion equation (2). Essentially most existing tracking techniques are banking on the diffusion tensor framework. However, it has been suggested to get around the inadequacy presented in DTI by using newly developed imaging approaches, like high angular resolution diffusion imaging (HARDI) [39]–[42], q-space imaging (QSI) [43], [44], or generalized diffusion tensor imaging (GDTI) [45], [46]. An outstanding feature of the fiber reconstruction method using diffusion simulations is that it can be seamlessly adapted to a platform established by the new imaging techniques. Studies have shown that the generalized diffusion tensor model

is able to not only accommodate HARDI and GDTI methods but QSI as well, due to the inherent relationships among DTI, HARDI, GDTI, and QSI [45], [46]. This makes it possible for the diffusion simulation-based tractography to become independent of the particular imaging techniques used to collect data. The proposed fiber tracking method may accommodate other diffusion imaging data by adopting a more sophisticated diffusion simulation, which is governed by a generalized diffusion equation associated with generalized diffusion tensors, according to a generalization of Fick's second law [45]. We are planning in the future work to develop an improved computational framework for building fiber connections that can solve the generalized diffusion equation.

As mentioned earlier, our algorithm presents a leap-frog tracking style which is not seen in most of the existing tracing techniques. This characteristic, however, raises challenge for the algorithm to work at a sub-voxel dimension, which usually is attained in other methods by doing interpolation or even constructing a continuous tensor field. As for the diffusion-based approach, increasing the data resolution is still a viable way to ease the restraint, though a few voxels have to be jumped over for each step moving forward no matter how fine the data grid is. Nevertheless, in what way the tracking results of the current algorithm are influenced by the interpolation is not clear and subject to further analysis. When the tensor data is interpolated to a higher resolution, another problem arises, where the increased computation burden cannot be underestimated. For example, the total running time for tracking the corpus callosum tract from splenium (Fig. 6) is about 293 min on an HP-UX machine with a 750 MHz PA-RISC 8700 processor. The reason lies in the fact that we have to carry out diffusion simulation for each of the diffusion roots and each of the simulations sweeps the whole brain volume. As to the current real data resolution (interpolated), it means the diffusion process has to be simulated on a $128 \times 128 \times 48$ grid, which is very time-consuming. And the number of diffusion roots determines how many such simulations need to be conducted. The improvement for the algorithm on computational cost has been under way, in which each diffusion simulation initiated from a root only spreads through its neighboring parts of the brain, expected to drastically reduce the running time down to a couple of minutes. In addition, the development of connectivity likelihood measures will be included in the future work to appraise the confidence in each of the computed fiber tracks by some quantitative way to see how each point along a path is connected to the starting voxel.

V. Conclusion

In summary, a novel white matter fiber tractography algorithm has been developed using diffusion tensor MRI. This algorithm is based on conducting consecutive simulations of anisotropic diffusion over datasets obtained from living human brain, which are utilized to construct three dimensional diffusion fronts. The fiber trajectories are constructed by evaluating the distance and orientation from fronts to their corresponding diffusion seeds. Synthetic tensor data has been generated to validate the algorithm. For the demonstration on real DT-MRI data several major white matter fiber pathways have been reconstructed, which are in agreement with the known anatomy and similar to those estimated by using other reported approaches. The ability to yield branching pathways is the primary advantage of the diffusion-based tractography presented in this work and it also has a greater potential to get through regions with crossing fibers and, thus, enhances robustness and reliability of the tracking process. Another desired feature of the algorithm is its capability of fitting into the environment of the generalized diffusion tensor imaging.

References

[1] C. Beaulieu, "The basis of anisotropic water diffusion in the nervous system—A technical review," *NMR Biomed.*, vol. 15, pp. 435–455, 2002.

[2] P. J. Basser, J. Mattiello, and D. L. Bihan, "Estimation of the effective self-diffusion tensor from the NMR spin echo," *J. Magn. Res. Ser. B*, vol. 103, pp. 247–254, 1994.

[3] C.-P. Lin, W.-Y. I. Tseng, H.-C. Cheng, and J.-H. Chen, "Validation of diffusion tensor magnetic resonance axonal fiber imaging with registered manganese-enhanced optic tracts," *NeuroImage*, vol. 14, pp. 1035–1047, 2001.

[4] P. J. Basser, S. Pajevic, C. Pierpaoli, J. Duda, and A. Aldroubi, "*In vivo* fiber tractography using DT-MRI data," *Magn. Reson. Med.*, vol. 44, pp. 625–632, 2000.

[5] T. E. Conturo, N. F. Lori, T. S. Cull, E. Akbudak, and A. Snyder, "Tracking neuronal fiber pathways in the living human brain," *Proc. Nat. Acad. Sci.*, vol. 96, pp. 10 422–10 427, 1999.

[6] D. K. Jones, A. Simmons, S. C. R. Williams, and M. A. Horsfield, "Non-invasive assessment of axonal fiber connectivity in the human brain via diffusion tensor MRI," *Magn. Reson. Med.*, vol. 42, pp. 37–41, 1999.

[7] S. Mori, W. E. Kaufmann, C. Davatzikos, B. Stieltjes, L. Amodei, K. Fredericksen, G. D. Pearlson, E. R. Melhem, M. Solaiyappan, G. V. Raymond, H. W. Moser, and P. C. M. van Zijl, "Imaging cortical association tracts in the human brain using diffusion-tensor-based axonal tracking," *Magn. Reson. Med.*, vol. 47, pp. 215–223, 2002.

[8] M. Lazar, D. M. Weinstein, J. S. Tsuruda, K. M. H. K. Arfanakis, M. E. Meyerand, B. Badie, H. A. Rowley, V. Haughton, A. Field, and A. L. Alexander, "White matter tractography using diffusion tensor deflection," *Hum. Brain Map.*, vol. 18, pp. 306–321, 2003.

[9] C. Poupon, C. A. Clark, V. Frouin, J. Regis, I. Bloch, D. L. Bihan, and J. Mangin, "Regularization of diffusion-based direction maps for the tracking of brain white matter fascicles," *NeuroImage*, vol. 12, pp. 184–195, 2000.

[10] C. Poupon, J. F. Mangin, C. A. Clark, V. Frouin, and J. Regis, "Toward inference of human brain connectivity from MR diffusion tensor data," *Med. Image Anal.*, vol. 5, pp. 1–15, 2001.

[11] M. R. Wiegell, H. B. Larsson, and V. J. Wedeen, "Fiber crossing in human brain depicted with diffusion tensor MR imaging," *Radiol.*, vol. 217, pp. 897–903, 2000.

[12] M. Björnemo, A. Brun, R. Kikinis, and C. F. Westin, "Regularized stochastic white matter tractography using diffusion tensor MRI," in *Proc. 5th Int. Conf. on Medical Image Computing and Computer-Assisted Intervention (MICCAI'02)*, Tokyo, Japan, 2002, pp. 435–442.

[13] C. Gössl, L. Fahrmeir, B. Pütz, L. M. Auer, and D. P. Auer, "Fiber tracking from dti using linear state space models: Detectability of the pyramidal tract," *NeuroImage*, vol. 16, pp. 378–388, 2002.

[14] P. Hagmann, J. P. Thiran, L. Jonasson, P. Vandergheynst, S. Clarke, P. Maeder, and R. Meuli, "DTI mapping of human brain connectivity: Statistical fiber tracking and virtual dissection," *NeuroImage*, vol. 19, pp. 545–554, 2003.

[15] M. A. Koch, D. G. Norris, and M. Hund-Georgiadis, "An investigation of functional and anatomical connectivity using magnetic resonance imaging," *NeuroImage*, vol. 16, pp. 241–250, 2002.

[16] G. J. M. Parker and D. C. Alexander, "Probabilistic Monte Carlo based mapping of cerebral connections utilising whole-brain crossing fiber information," in *Lecture Notes in Computer Science*, C. Taylor and A. Noble, Eds. Berlin, Germany: Springer, 2003, vol. 2737, pp. 684–695.

[17] G. J. M. Parker, C. A. M. Wheeler-Kingshott, and G. J. Barker, "Estimating distributed anatomical connectivity using fast marching methods and diffusion tensor imaging," *IEEE Trans. Med. Imag.*, vol. 21, no. 5, pp. 505–512, May 2002.

[18] J.-D. Tournier, F. Calamante, D. G. Gadian, and A. Connelly, "Diffusion-weighted magnetic resonance imaging fiber tracking using a front evolution algorithm," *NeuroImage*, vol. 20, pp. 276–288, 2003.

[19] L. Jonasson, P. Hagmann, X. Bresson, R. Meuli, O. Cuisenaire, and J.-P. Thiran, "White matter mapping in DT-MRI using geometric flows," in *Proc. 9th Int. Workshop on Computer Aided Systems Theory*, Las Palmas de Gran Canaria, Spain, 2003, pp. 80–82.

[20] J. S. W. Campbell, K. Siddiqi, B. C. Vemuri, and G. B. Pike, "A geometric flow for white matter fiber tract reconstruction," in *Proc. IEEE Int. Symp. Biomedical Imaging Conf.*, 2002, pp. 505–508.

[21] C. Lenglet, R. Deriche, and O. Faugeras, "Inferring white matter geometry from diffusion tensor MRI: Application to connectivity mapping," in *Lecture Notes in Computer Science*, T. Pajdla and J. Matas, Eds. Berlin, Germany: Springer, 2004, vol. 3024, pp. 127–140.

[22] L. O'Donnell, S. Haker, and C. F. Westin, "New approaches to estimation of white matter connectivity in diffusion tensor MRI: Elliptic PDE's and geodesics in a tensor-warped space," in *Proc. 5th Int. Conf. Medical Image Computing and Computer-Assisted Intervention (MICCAI'02)*, Tokyo, Japan, 2002, pp. 459–466.

[23] P. G. Batchelor, D. L. G. Hill, F. Calamante, and D. Atkinson, "Study of connectivity in the brain using the full diffusion tensor from MRI," *Lecture Notes in Computer Science*, vol. 2082, pp. 121–133, 2001.

[24] D. Gembris, H. Schumacher, and D. Suter, "Solving the diffusion equation for fiber tracking in the living human brain," in *Proc. Int. Soc. Magn. Reson. Med.*, 2001, p. 1529.

[25] P. G. Batchelor, D. L. G. Hill, D. Atkinson, F. Calamante, and A. Connelly, "Fiber-tracking by solving the diffusion-convection equation," in *Proc. Int. Soc. Magn. Reson. Med.*, 2002, p. 1135.

[26] E. O. Stejskal and J. E. Tanner, "Spin diffusion measurements: Spin echoes in the presence of a time-dependent field gradient," *J. Chem. Phys.*, vol. 42, pp. 288–292, 1965.

[27] F. Calamante, D. A. Porter, D. G. Gadian, and A. Conelly, "Correction for eddy-current induced b_0 shifts in diffusion-weighted echo-planar imaging," *Magn. Reson. Med.*, vol. 41, pp. 95–102, 1999.

[28] E. Plante and L. Turkstra, "Sources of error in the quantitative analysis of MRI scans," *Magn. Reson. Imag.*, vol. 9, pp. 589–595, 1991.

[29] H. Zhang, P. A. Yushkevich, and J. C. Gee, "Registrtaion of diffusion tensor images," in *Proc. IEEE Comp. Soc. Conf. Computer Vision and Pattern Recognition*, vol. 1, Washington, DC, 2004, pp. 842–847.

[30] C. Nicholson, "Diffusion and related transport mechanism in brain tissue," *Rep. Prog. Phys.*, vol. 64, pp. 815–884, 2001.

[31] N. Kang, J. Zhang, and E. S. Carlson, "Performance of ILU preconditioning techniques in simulating anisotropic diffusion in the human brain," *Future Gen. Comput. Syst.*, vol. 20, pp. 687–698, 2004.

[32] N. Kang, J. Zhang, and E. Carlson, "Parallel simulation of anisotropic diffusion with human brain DT-MRI data," *Comput. Structures*, vol. 82, pp. 2389–2399, 2004.

[33] C. Pierpaoli and P. J. Basser, "Toward a quantitative assessment of diffusion anisotropy," *Magn. Reson. Med.*, vol. 36, pp. 893–906, 1996.

[34] H. Gudbjartsson and S. Patz, "The Rician distribution of noisy MRI data," *Magn. Reson. Med.*, vol. 34, pp. 910–914, 1995.

[35] C.-F. Westin, S. E. Maier, H. Mamata, A. Nabavi, F. A. Jolesz, and R. Kikinis, "Processing and visualization for diffusion tensor MRI," *Med. Image Anal.*, vol. 6, pp. 93–108, 2002.

[36] J. Hanaway, *The Brain Atlas: A Visual Guide to the Human Central Nervous System*. Bethesda, MD: Fitzgerald, 1998.

[37] T. H. Williams, N. Gluhbegovic, and J. Y. Jew. (1999) The Human Brain: Dissections of the Real Brain. The University of Iowa. [Online]. Available: http://www.vh.org/adult/provider/anatomy/BrainAnatomy/BrainAnatomy.html

[38] M. Catani, R. J. Howard, S. Pajevic, and D. K. Jones, "Virtual *in vivo* interactive dissection of white matter fasciculi in the human brain," *NeuroImage*, vol. 17, pp. 77–94, 2002.

[39] D. C. Alexander, G. J. Barker, and S. R. Arridge, "Detection and modeling of non-Gaussian apparent diffusion coefficient profiles in human brain data," *Magn. Reson. Med.*, vol. 48, pp. 331–340, 2002.

[40] A. L. Alexander, K. M. Hasan, M. Lazar, J. S. Tsuruda, and D. L. Parker, "Analysis of partial volume effects in diffusion-tensor MRI," *Magn. Reson. Med.*, vol. 45, pp. 770–780, 2001.

[41] L. R. Frank, "Characterization of anisotropy in high angular resolution diffusion-weighted MRI," *Magn. Reson. Med.*, vol. 47, pp. 1083–1099, 2002.

[42] D. S. Tuch, T. G. Reese, M. R. Wiegell, N. Makris, J. W. Belliveau, and V. J. Wedeen, "High angular resolution diffusion imaging reveals intravoxel white matter fiber heterogeneity," *Magn. Reson. Med.*, vol. 48, pp. 577–582, 2002.

[43] C.-P. Lin, V. J. Wedeen, J.-H. Chen, C. Yao, and W.-Y. Tseng, "Validation of diffusion spectrum magnetic resonance imaging with manganese-enhanced rat optic tracts and *ex vivo* phantoms," *NeuroImage*, vol. 19, pp. 482–495, 2003.

[44] D. S. Tuch, T. G. Reese, M. R. Wiegell, and V. J. Wedeen, "Diffusion mri of complex neural architecture," *Neuron*, vol. 40, pp. 885–895, 2003.

[45] C. Liu, R. Bammer, B. Acar, and M. E. Moseley, "Characterizing non-Gaussian diffusion by using generalized diffusion tensors," *Magn. Reson. Med.*, vol. 51, pp. 924–937, 2004.

[46] E. Özarslan and T. H. Mareci, "Generalized diffusion tensor imaging and analytical relationships between diffusion tensor imaging and high angular resolution diffusion imaging," *Magn. Reson. Med.*, vol. 50, pp. 955–965, 2003.